Linear, resistive stability studies for Wendelstein 7-X-type equilibria with external current drive

E. Strumberger[1], S. Günter[1], and the Wendelstein 7-X Team[2*]
[1]Max Planck Institute for Plasma Physics, Boltzmannstr. 2.
85748 Garching, Germany
[2]Max Planck Institute for Plasma Physics, Wendelsteinstr. 1.
17491 Greifswald, Germany

September 8, 2020

Abstract

Comprehensive linear stability studies of resistive modes are presented for Wendelstein 7-X-type stellarator equilibria with electron cyclotron current drive (ECCD). The external co-current drive leads to an increase of the rotational transform and the formation of one or two $\iota = 1$ rational flux surfaces. Using the 3D linear stability CASTOR3D code, low n^*-type resistive modes (n^*=1,2...,8 with n^* being the dominant toroidal Fourier harmonic contributing to the mode) are investigated. We studied the dependence of their growth rates on plasma resistivity, parallel viscosity, and shape of the rotational transform profile (especially various distances between two ι=1 flux surfaces). Similarly to tokamak configurations, single and double tearing modes, and internal resistive kink modes are found. In addition, modes oscillating between two n^*-types of the same mode family are observed. The frequencies of those modes are in the range of ≈10-260 Hz. Equilibria with either a large distance between the ι=1 flux surfaces, or a single ι=1 surface are most unstable with respect to n^*=1 resistive kink modes. The latter finding fits to the experimental observation of sawtooth-like oscillations followed by a thermal quench in W7-X discharges with ECCD.

Keywords: Stellarator equilibria, linear stability, double tearing modes, resistive kink modes, Wendelstein 7-X

*For the Wendelstein 7-X Team see the author list: T. Klinger et al., Nuclear Fusion **59** (2019) 112004, doi.org./10.1088/1741-4326/ab03a7

email address of the corresponding author: erika.strumberger@ipp.mpg.de (E. Strumberger)

(The figures appear in colour only in the electronic version)

1 Introduction

The Wendelstein 7-X stellarator (W7-X) started successful operation in 2015 [1, 2]. Electron cyclotron resonance heating (ECRH) [3] is an integral part of its start-up and operation phases. ECRH is used for steady-state heating, and it allows also for co- and counter electron-cyclotron current drive (ECCD). Particularly, experiments with strong central co-ECCD show sawtooth like oscillations followed by a sudden decrease of the central electron temperature [2, 4]. While a finite bootstrap current almost completely balances the current driven by counter-ECCD, both currents sum up in case of co-ECCD. W7-X was optimized with respect to almost current-free plasmas (small boostrap current), and magnetic fields characterized by monotonic, low-shear rotational transform profiles (ι-profiles) slightly below or above $\iota = 1$, but without low-order rational values inside the plasma [5]. The above mentioned experiments have been performed to investigate the effect of additional current drive.

Numerous linear (e.g. MARS [6]), CarMa [7], MISHKA-F [8], etc.) and non-linear stability codes (e.g. JOREK [9], M3D-C1 [10], XTOR [11], etc.) are available to investigate the stability of axisymmetric equilibria taking into account important physical effects such as resistivity, viscosity, diamagnetic drift, etc.. However, for 3D plasma configurations the situation is different. There are a few ideal linear stability codes, such as CAS3D [12], or TERPSICHORE [13], but the CASTOR3D code is the only 3D linear resistive code available. Usually, the 3D linear stability CAS3D code based on the energy principle is used to investigate the ideal stability properties of W7-X equilibria. For example, these studies showed that the so-called low-iota case with 5/6 islands outside the plasma is unstable with respect to free-boundary perturbations even at low plasma beta ($< \beta >= 0.9\%$) [14]. However, no ideal modes could be found for the W7-X discharges with current-drive mentioned above, whether with the CAS3D code [15] nor the CASTOR3D code. This is not surprising because ideal modes, such as ideal kink or "infernal" modes (low-shear kink modes) require a high plasma beta to become unstable [16, 17]. The considered W7-X discharges are low-β plasmas with a volume averaged plasma beta of $< \beta >= 0.26\%$. Therefore, the CASTOR3D code is used to investigate the stability of these discharges with respect to resistive modes.

The CASTOR3D code is based on the full MHD equations and allows to study the stability properties of 3D equilibria, taking into account plasma resistivity and parallel viscosity. Starting with a realistic current-free W7-X-type equilibrium, a set of equilibria with small toroidal currents simulating central co-ECCD is designed by slight changes of the originally monotonic ι-profile. The considered ι-profiles are non-monotonic and have various distances between the two ι=1 rational flux surfaces. The stability properties of these equilibria with respect to low n^*-type resistive modes (n^*=1,2,...,8 with n^* being the dominant toroidal Fourier harmonic contributing to the mode [18]) are studied, assuming different values of plasma resistivity and viscosity. Similarly to tokamak configurations, single and double tearing modes, and internal resistive kink modes are found. In addition, modes oscillating between two n^*-types of the same mode family are observed. Their frequencies are in the range of ≈10-260 Hz. Especially, the finding of n^*=1 resistive kink modes fits to the experimental observation of sawtooth-like oscillations followed by a thermal quench [2, 4]. Our studies show that these kink modes are the most unstable modes of equilibria with either a large distance between the ι=1 flux surfaces, or a single ι=1 surface.

The paper is organized as follows. The properties of the underlying W7-X type equilibrium and the modifcations of its rotational transform profile are described in section 2. Resistive stability studies are subject of section 3. There, the stability properties of the three mode families [12] of the five-periodic W7-X stellarator equilibria are discussed in detail in subsections 3.1 - 3.3. A summary of the results and conclusions are presented in section 4. Finally, some numerical details are discussed in the appendix.

2 Plasma equilibria

The following studies are based on a realistic W7-X-type equilibrium[1]. This current-free equilibrum has a volume-averaged plasma beta of $< \beta >= 0.26\%$, and a plasma pressure of $p_a = 16.3$ kPa at the magnetic axis. Cross-sections of its flux surfaces are presented at three toroidal angles ($\varphi = 0^{\rm o}, 18^{\rm o}$ and $36^{\rm o}$) in figure 1. The monotonic rotational transform profile and the normalized pressure profile of this equilibrium are shown in figures 2(a)-(b). There, also the assumed particle density profile, and the resulting temperature profile are illustrated. For the stability studies we use a particle density of $n_a = 0.25 \cdot 10^{20}$ m^{-3} at the magnetic axis.

[1] W7-X discharge 20171207.006 [4]

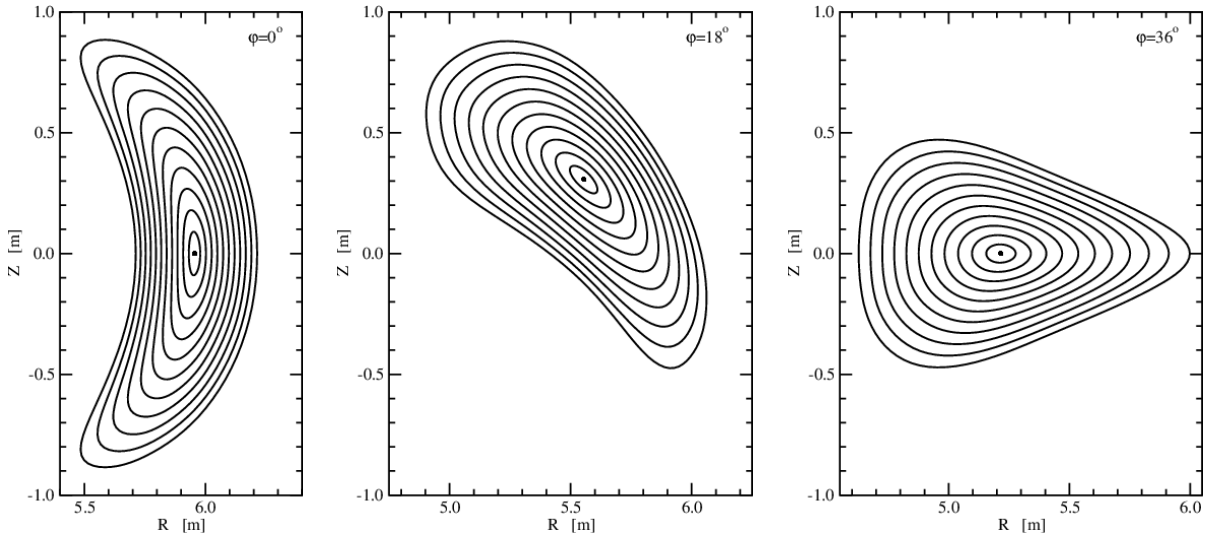

Figure 1: *Cross-sections of the W7-X equilibrium at the toroidal angles φ =0, 18 and 36°.*

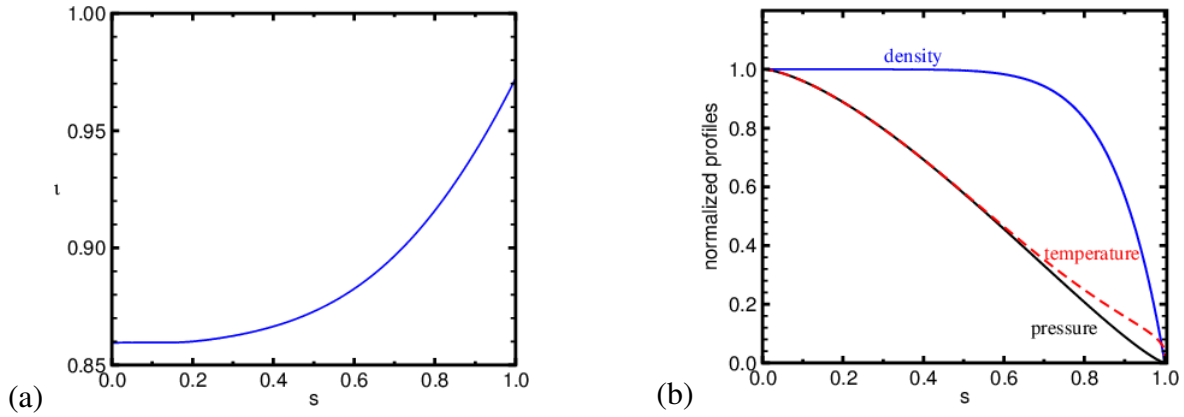

(a) (b)

Figure 2: *(a) Rotational transform profile, and (b) normalized profiles of pressure, particle density and temperature as functions of the square root of the normalized toroidal flux, s.*

In order to simulate non-monotonic rotational transform profiles that may be created in co-ECCD experiments [2, 4], the monotonic ι-profile is modified by adding an analytical function as described in the appendix. By varying the parameters of this function, two sets of non-monotonic profiles are produced. Figures 3(a)-(b) show a representative selection of these profiles. They have one or two $\iota = 1$ flux surfaces. The radial position of the maximum ι-value has been kept fixed for the first set of profiles (figure 3(a)), while this position has been shifted towards the magnetic axis for the second set (figure 3(b)). Besides the modified profiles, also the initial monotonic ι-profile is shown in figures 3(a)-(b). In contrast to tokamak profiles, this profile increases from the plasma centre towards the plasma boundary, because in a stellarator, such as W7-X, the toroidal and the poloidal fields are produced by external coils only. Further-

more, all profiles are very flat. Note, here and in the following the radial coordinate s denotes the square root of the normalized toroidal flux.

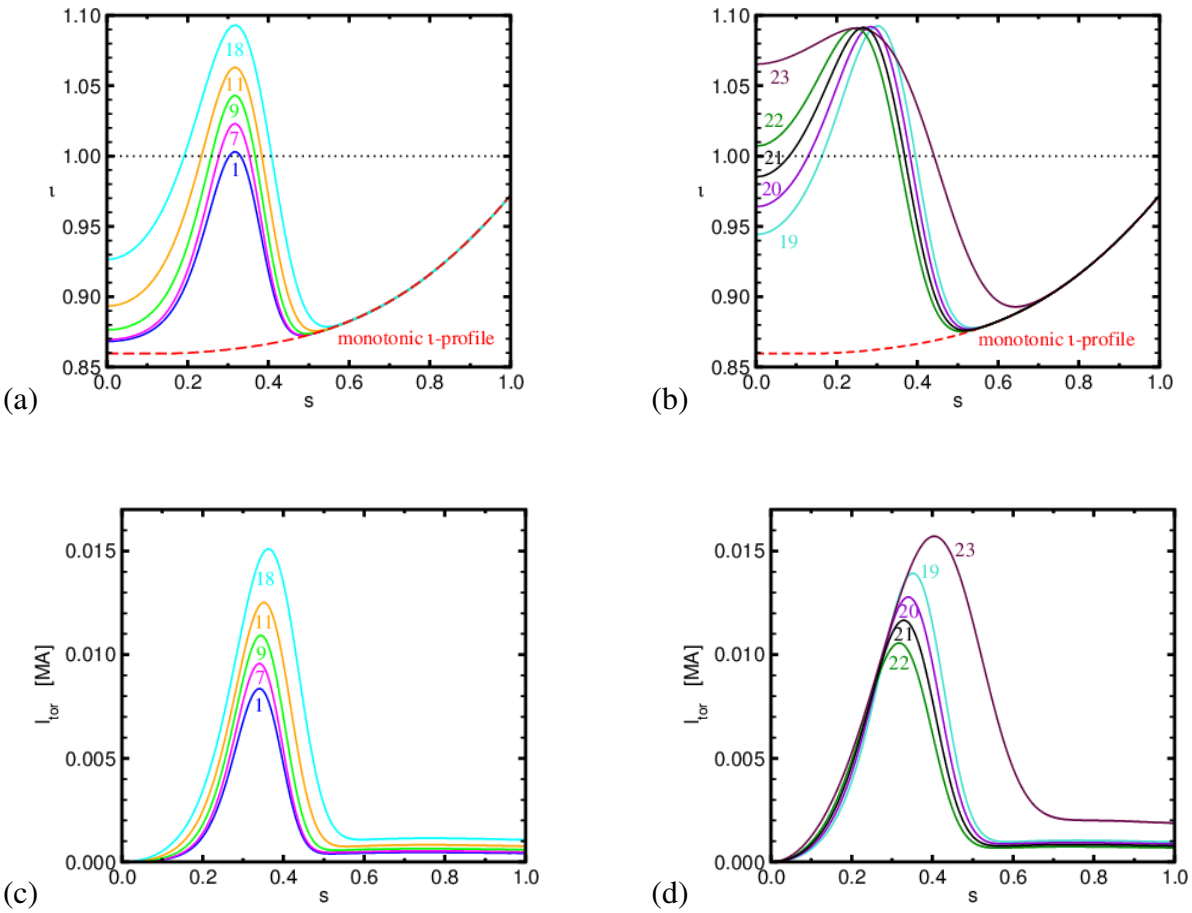

Figure 3: *Various ι-profiles with (a) fixed, and (b) shifted maximum positions, and (c,d) their corresponding toroidal current profiles, I_{tor}.*

Using the VMEC equilibrium code [19], central co-ECCD is simulated by computing fixed-boundary equilibria for the modified rotational transform profiles. Plasma boundary, pressure profile, and total toroidal flux are kept fixed for all equilibria. The resulting toroidal current profiles, I_{tor}, are shown in figures 3(c)-(d).

3 Resistive stability studies

For the first time, comprehensive linear stability studies of resistive modes are presented for W7-X-type stellarator equilibria. The growth rates of low n^*-type modes are computed for various

resistivities, parallel ion viscosities, and ι-profiles with different distances bewteen the ι=1 flux surfaces. The normalized resistivity profile, $\frac{\eta}{\eta_a}$ (η_a being the resistivity at the magnetic axis), is calculated from the normalized electron temperature profile using the Spitzer formula. Since the assumed profiles shown in figure 2(b) are zero at the plasma boundary (for ion and electron temperatures the same normalized profiles are assumed), the Spitzer resistivity would go to infinity. To avoid this singularity a small value of 0.1 is added to the normalized temperature profile. In the plasma centre the resulting modified resistivity profile is a good approximation to the Spitzer profile, but it has a numerically manageable finite value at the plasma boundary as shown in figure 4.

The resistive layer width of a tearing mode shrinks with decreasing resistivity. That is, a small resistivity requires a high numerical resolution in radial direction (see appendix). Therefore, the computations have been limited to $\eta_a \gtrsim 1 \cdot 10^{-8}$ Ωm, which corresponds to a Lundquist number [20] of $S = (\mu_0 a v_A)/\eta = 5.33 \cdot 10^8$ (μ_0=permeability, a=0.55 m minor radius, and $v_A = 7.7 \cdot 10^6 \frac{\mathrm{m}}{\mathrm{s}}$ Alfvén velocity). Electron temperatures of several keV have been observed in W7-X discharges with ECCD [4]. Due to the Spitzer formula, such high temperatures would imply smaller resistivities (e.g. T_e=3 keV corresponds to $\eta_a = 5 \cdot 10^{-9}\Omega$m). However, besides the numerical limits also the range of validity of the applied single-fluid magnetohydrodynamic model is restricted with respect to the resistivity. If the ion sound Larmour radius, ρ_s, is comparable or even larger than the resistive layer width, two-fluid effects become important [21]. For the considered cases, ion sound Larmour radius and resistive layer width become comparable for resistivities in the order of $\eta_a \lesssim 10^{-8}$ Ωm (see appendix).

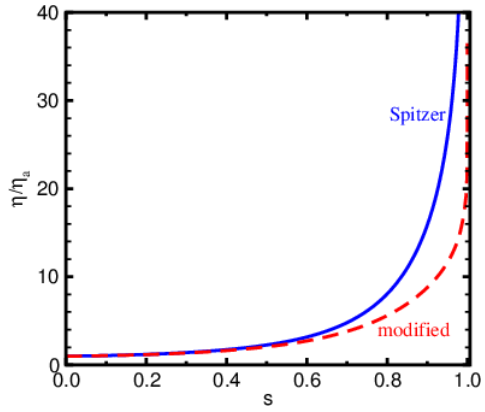

Figure 4: *Normalized Spitzer resistivity profile (blue, solid line) corresponding to the normalized temperature profile shown in Fig. 2b, and modified profile (red, dashed line) used for the stability calculations.*

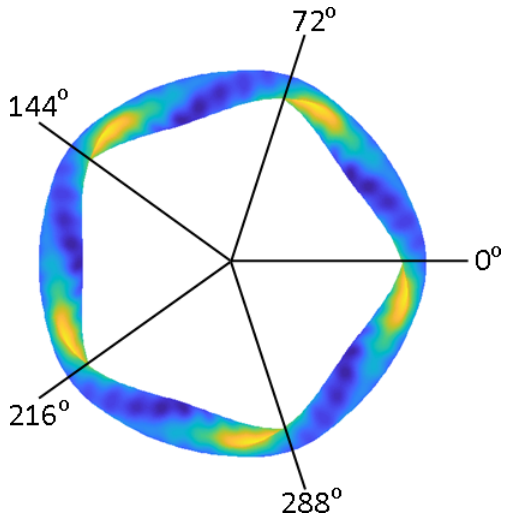

Figure 5: *Plasma geometry of the W7-X equilibrium with the colours indicating the magnetic field strength at the plasma boundary (2.1 (dark blue) $\leq B \leq$ 2.9 T (yellow)).*

The Wendelstein 7-X stellarator has five field periods (N_p=5). Figure 5 shows the plasma geometry of the W7-X-type equilibrium described in the previous section. The colours indicate the magnetic field strength at the plasma boundary. Viewing from above, the toroidal angle of $\varphi = 0^{\text{o}}$ corresponds to the so-called bean-shaped cross-section of the first period, while the triangular cross-section is located at $\varphi = 36^{\text{o}}$ (see figure 1). As explained in detail in [12], the fivefold symmetry of the equilibrium implies the existence of three mode families:

mode family 0: n=0,5,10,15,20,25,...

mode family 1: n=1,4,6,9,11,14,...

mode family 2: n=2,3,7,8,12,13,...

That is, only toroidal harmonics which belong to the same mode family yield non-vanishing coupling terms. This partial decoupling of the toroidal harmonics allows us to study the stability properties of each mode family separately. The poloidal and toroidal Fourier spectra used for the following calculations are listed in the appendix. We restrict our considerations to low-n^* modes with $1 \leq n^* \leq 8$. While only a single toroidal harmonic contributes to a mode of an axisymmetric equilibrium (these modes are characterized by n, e.g. n=1 mode), several n-harmonics couple together and contribute to the Fourier spectrum of the perturbation in case of 3D equilibria. Therefore, we choose the dominant (most contributing) n-harmonic of a perturbation Fourier spectrum , which we name n^*, to characterize a stellarator mode [18].

3.1 Mode family 0

At first, we investigate the stability properties of W7-X-type equilibria with external current drive for mode family 0. Using a small, but numerically not too demanding resistivity of $\eta_a =$

$1 \cdot 10^{-7}$ Ωm, and no viscosity, the growth rate of the n^*=5 double tearing mode (DTM) is computed as function of the distance between the two ι=1 flux surfaces, Δs (for the used ι-profiles see figure 3(a)). As illustrated in figure 6, the growth rate shows a similar dependence on Δs, as it is already well known for tokamaks [22]. It increases with growing distance up to a maximum value, and then it decreases. However, because of the 3D geometry, the eigenvalues of the two orthogonal solutions of each mode may be different.

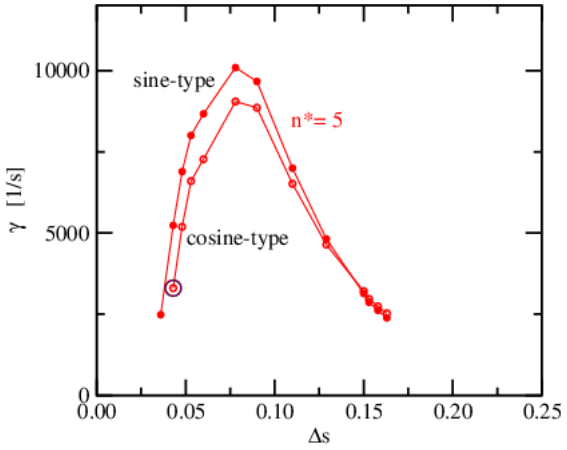

Figure 6: *Growth rates of the n^*=5, sine- and cosine-type modes as functions of the distance between the two ι=1 rational flux surfaces, Δs. The brown circle marks an overstable mode.*

The sine- and cosine-type characters of the two orthogonal solutions are illustrated in figure 7. The CASTOR3D codes uses complex, $\exp(2\pi i(mu+nv))$, and conjugate-complex exponential functions, $\exp(-2\pi i(mu+nv))$, for the Fourier representation of the perturbed quantities, with u and v being the poloidal and toroidal coordinates [23, 18], respectively. Due to the stellarator symmetry of W7-X, these exponential functions combine to pure sine- and cosine-type functions, if the growth rates of the orthogonal solutions are different. Since the modes of mode family 0 match the five periods of W7-X, the differences are quite distinctive for the n^*=5 double tearing modes, especially for small distances, Δs. Figures 7(a) and 7(b) show the Fourier spectra of the real part of the radial velocity perturbation for the cosine- and sine-type n^*=5 modes, respectively. The radial distance of the ι=1 flux surfaces amounts to Δs=0.078. Because of the 3D geometry also the n=0,10,15,... harmonics contribute to the modes. The Fourier spectra are characteristic of asymmetrically coupled tearing modes, as illustrated in the sketch (figure 7(c) (middle)). There, the X- and O-points of the coupled islands face each other.

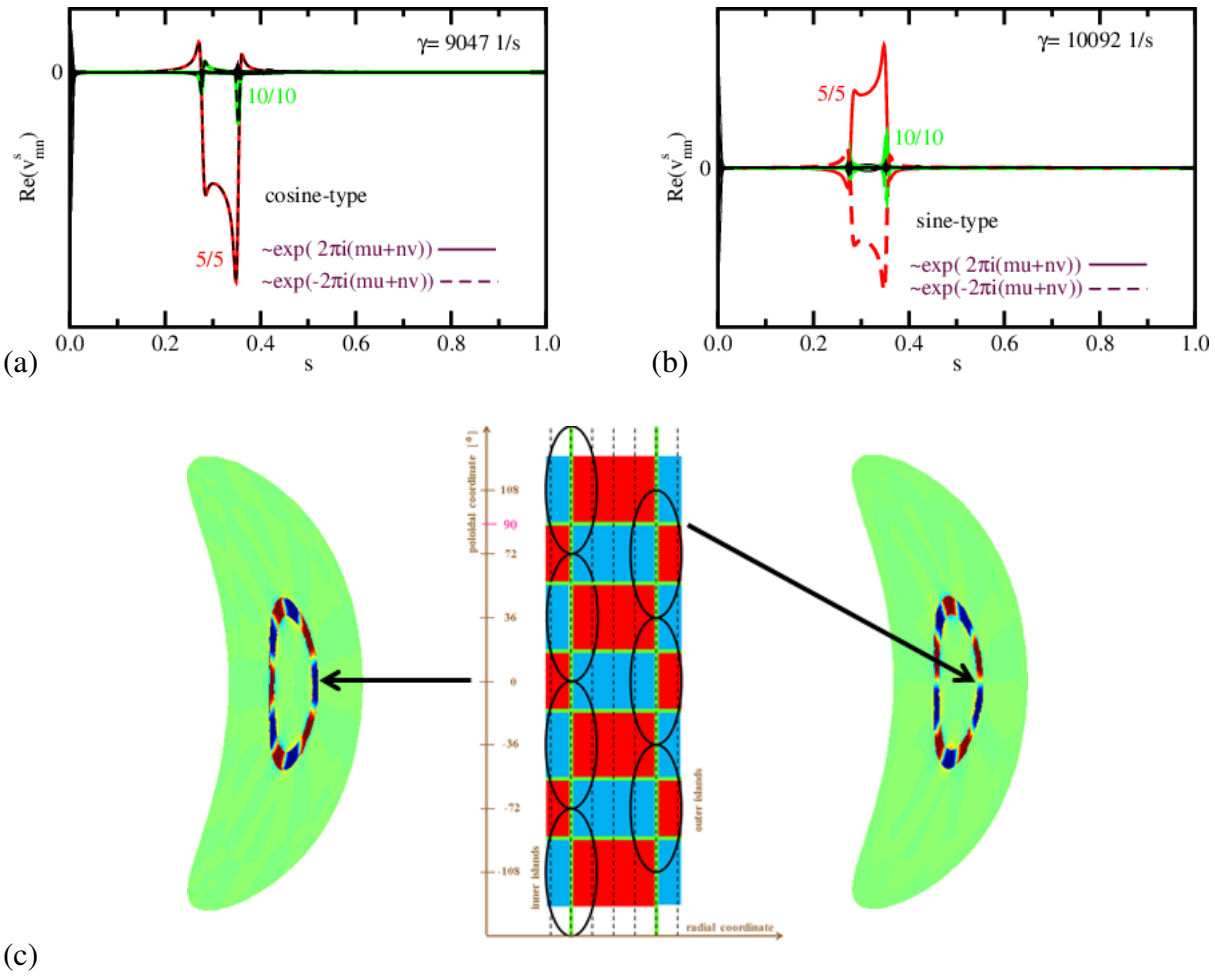

Figure 7: *Fourier spectra of the real part of the radial velocity perturbation of (a) the cosine- and (b) the sine-type n^*=5 DTM for Δs=0.078. The solid and dashed lines denote the contributions of the complex and conjugate-complex eigenfunctions, respectively. The largest contributions are marked by their toroidal and poloidal harmonics, n/m. (c) Corresponding mode structures at the bean-shaped cross-sections, and sketch of the island positions. The colours indicate the radial displacement of the flux surfaces, that is, outward shift (red), inward shift (blue), and no shift (green) with respect to the unperturbed flux surfaces (vertical dashed lines in the sketch).*

In figure 7(c) (middle), the shift of flux surfaces due to the island formation is sketched. Using the same colour code, the structure of the radial velocity perturbation is shown for the cosine-type (figure 7(c) (left)) and the sine-type (figure 7(c) (right)) n^*=5 DTMs at the bean-shaped cross-section.

Since the CASTOR3D code solves a complex eigenvalue problem with eigenvalue $\lambda = \gamma + i\omega$ (γ being the growth rate, and ω being the oscillation frequency) also so-called overstable solutions

are possible. Such modes grow exponentially and oscillate simultaneously [24]. Here and in the following, overstable modes are marked by brown circles. In case of the cosine-type mode indicated in figure 6, the mode oscillates with a frequency of $\nu = \frac{\omega}{2\pi} = 96$ Hz between a cosine-type n^*=5 and a cosine-type n^*=10 mode structure. Such kind of oscillation will be discussed in more detail in the following section.

3.2 Mode family 1

Mode family 1 is more interesting with respect to possible sawtooth oscillations because it includes n^*=1 modes. Figure 8 shows the growth rates of n^*=1,4, and 6 resistive modes as functions of Δs. Values of $\Delta s \leq 0.218$ belong to the first set of ι-profiles (figure 3(a), profiles 1-18), while larger distances belong to the second set (figure 3(b), profiles 19-21). In contrast to modes of mode family 0, which match the five-fold periodicity of W7-X, the growth rates of the two orthogonal solutions are mostly the same (within the numerical accuracy) for modes of mode family 1 and 2. Therefore, only one solution is considered in the following. If the orthogonal solutions are degenerated, the complex and conjugate-complex eigenfunctions may not add up to pure sine- or cosine-type functions, but to any arbitrary combination, as illustrated in figure 9.

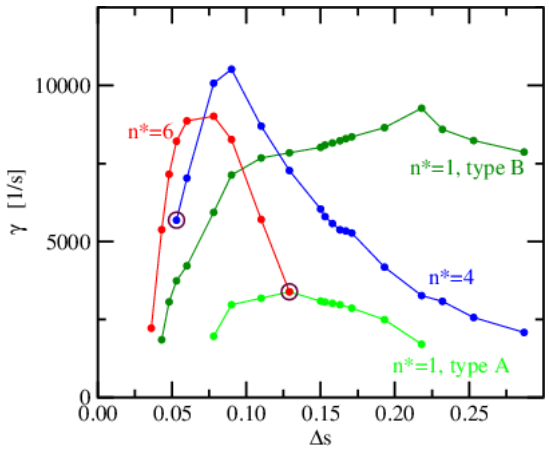

Figure 8: *Growth rates of the n^*=1,4, and 6 resistive modes as functions of Δs for $\eta_a = 1 \cdot 10^{-7}$ Ωm. The brown circles mark overstable modes.*

As shown in figure 8, two types of n^*=1 modes exist. Type A is a symmetrically coupled double tearing mode with the inner tearing mode corresponding to a resistive kink mode as illustrated in figure 9(a). In case of symmetrically coupled double tearing modes, the O-points of the coupled islands face each other. The symmetrically coupled n^*=1 modes are less unstable than the asymmetrically coupled ones (type B).

n^*=1, type A DTM

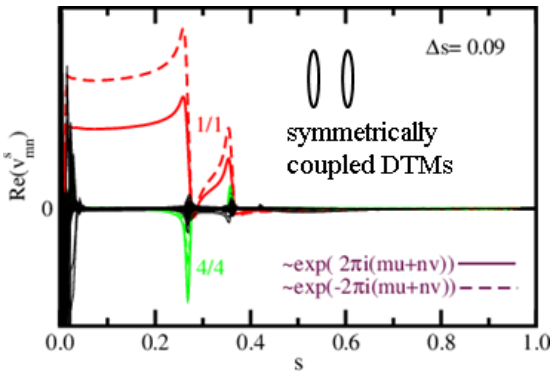

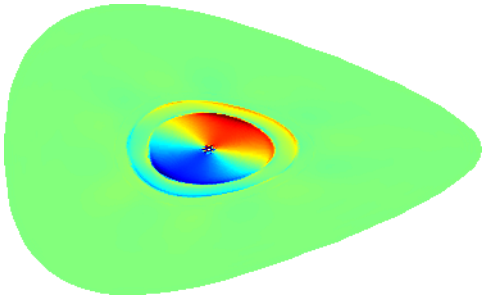

(a)

n^*=1, type B DTM

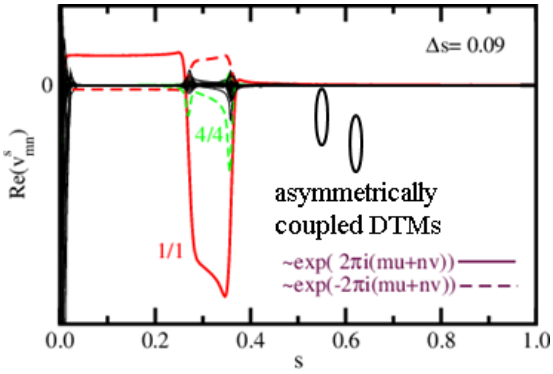

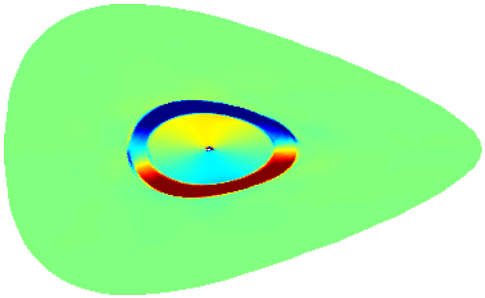

(b)

n^*=1, hybrid mode of type B DTM and resistive kink mode

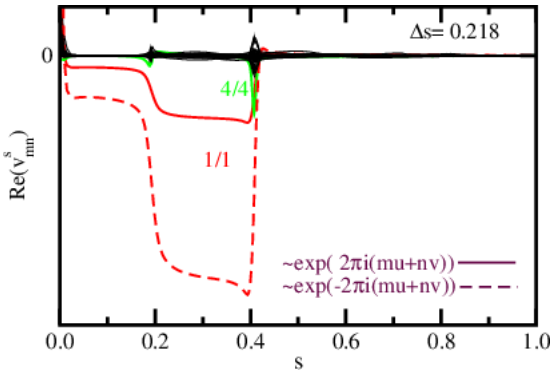

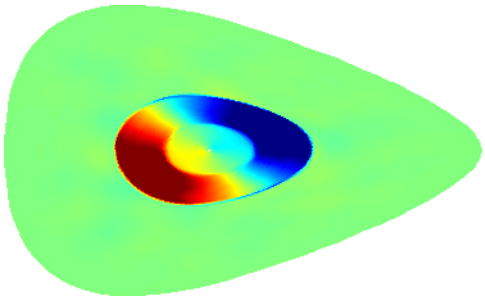

(c)

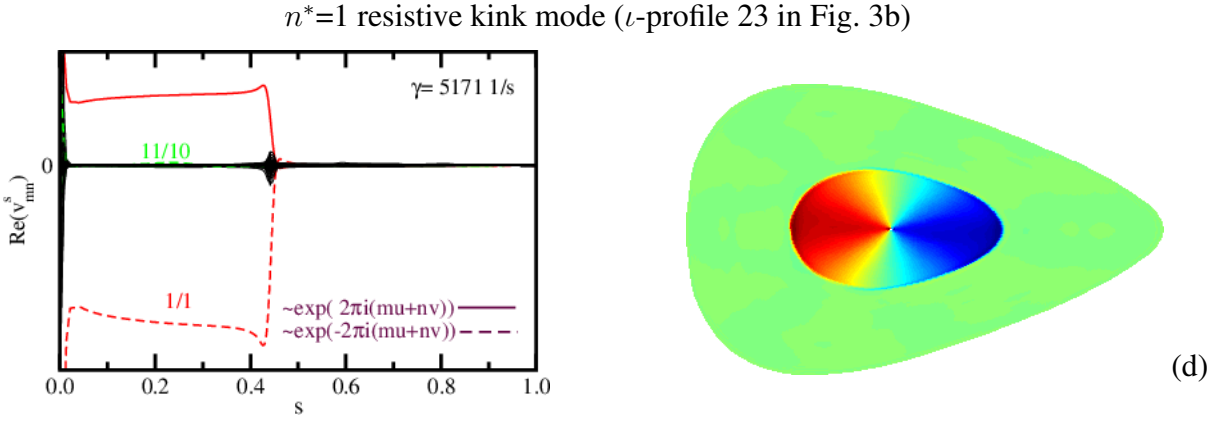

Figure 9: *Fourier spectra of the real part of the radial velocity perturbation (left columns) and corresponding mode structures (right columns) of n^*=1 modes for various distances between the ι=1 flux surfaces (a)-(c), and for a rotational transform profile with a single ι=1 surface (d).*

Figures 9(b)-(d) illustrate the Fourier spectra and the structures of the radial velocity perturbation of n^*=1 resistive modes for small and large distances between the $\iota = 1$ flux surfaces (figure 9(b) and 9(c)), and a ι-profile with only one $\iota = 1$ surface (figure 9(d)). With increasing Δs, the mode structure changes from a DTM to a single resistive kink mode.

Especially, Figs 9(a) and (b) show large fluctuations at the magnetic axis. These fluctuations, however, are not a result of the solution of the eigenvalue problem, and therefore, do not influence the eigenvalue. In fact, these fluctuations are a result of the special representation of the perturbations which has been chosen. In order to visualize the characteristic of an n^*=1 internal kink mode (finite perturbation at the magnetic axis), we do not show the Fourier harmonics of the eigenfunction of the radial velocity perturbation, $\hat{v}^s_{mn}(s)$, but the Fourier harmonics of the real part of the radial perturbation, $v^s_{mn}(s)$, itself. The radial perturbation is related with the corresponding eigenfunction by

$$v^s(s,v,u) = \frac{R^2}{\sqrt{g}}\hat{v}^s(s,v,u)$$

$$= \frac{R^2}{\sqrt{g}}\sum_{m,n}\hat{v}^s_{mn}(s)exp(2\pi i(mu+nv)) + \hat{\bar{v}}^s_{mn}(s)exp(-2\pi i(mu+nv)), \qquad (1)$$

with u and v being the poloidal and toroidal angle-like coordinates, R being the radial, cylindrical coordinate, and $\sqrt{g}$ being the Jacobian (for more details see [23]). The computation of $v^s(s,v,u)$ requires a division of the eigenfunction by the Jacobian. Since both quantities, eigenfunction and Jacobian, go to zero at the magnetic axis, small numerical inaccuracies may lead to

large fluctuations, which can be observed in some of the figures showing the Fourier spectrum of the real part of the radial velocity perturbation.

Figure 10(a) shows the growth rates of the n^*=1,4 and 6 DTMs as functions of the plasma resistivity for $\Delta s = 0.09$. As in axisymmetric configurations, the growth rates obey typical scalings [25, 22] within certain resistivity ranges. The n^*=1 DTM scales with $\gamma \propto \eta^{1/3}$ for $\eta < 6 \cdot 10^{-7}$ Ωm, while the growth rates of the n^*=4 and n^*=6 DTMs exhibit the $\gamma \propto \eta^{3/5}$ scaling for $\eta < 1 \cdot 10^{-7}$ Ωm and $\eta < 5 \cdot 10^{-8}$ Ωm, respectively. The growth rate of a single resistive kink mode as function of the resistivity is presented in figure 10(b). In the considered resistivity range, this growth rate increases with a gradient lying in between the two scalings.

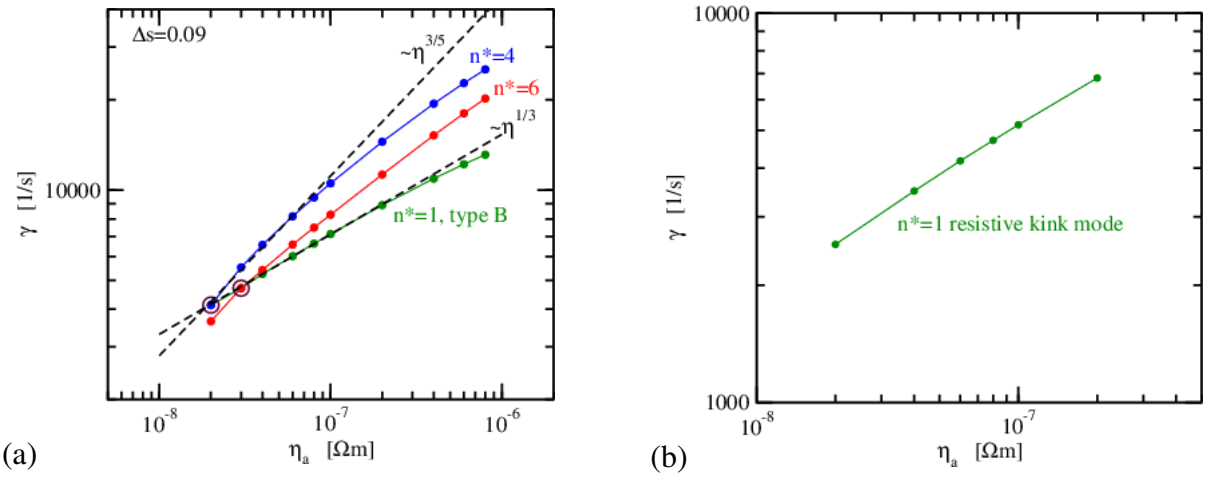

Figure 10: *(a) Growth rates of the n^*=1,4 and 6 DTMs as functions of η_a for $\Delta s = 0.09$. (b) Growth rate of the n^*=1 resistive kink mode as function of η_a for a ι-profile with only one ι=1 surface (profile 23, figure 3(b)). In both cases no viscosity is taken into account. The black dashed lines indicate the scalings $\gamma \propto \eta^{3/5}$ and $\gamma \propto \eta^{1/3}$.*

Within all three mode families overstable modes are observed (see figures 6, 8, 10(a), 12, 13, 16(a), and 17). Such oscillating solutions are found for tokamak equilibria, when the growth rates of differently coupled tearing modes of equal n-type coalesces (e.g. for a certain resistivity range [24]). They are called "overstable" in order to express the fact that the direction of the restoring force is opposite to the displacement. However, the restoring force is too big and so the resulting motion overshoots and results again in an instability [26]. In 3D configurations overstable modes are also possible, when the growth rates of two different n^*-type modes of the same mode family become equal. For example, as shown in figure 10(a), the growth rate of the n^*=1-type B mode coincides with the growth rate of the n^*=6 mode for $\eta_a = 3 \cdot 10^{-8}$ Ωm, and with the growth rate of the n^*=4 mode for $\eta_a = 2 \cdot 10^{-8}$ Ωm. In both cases, the solution of the

eigenvalue problem yields four solutions with equal growth rates (real part of the eigenvalue), and pairs of oscillation frequencies (imaginary part of the eigenvalue) with equal amount, but opposite signs. All four solutions correspond to modes oscillating between two n^*-types. As representative example, the oscillation between the n^*=1 and the n^*=4 DTM mode structures is illustrated in figure 11.

The first and second columns of figure 11 show the mode structures at the five triangular cross-sections at time $t = 0$ (first column) and $t = \frac{1}{4}T$ (second column), with $T = \frac{2\pi}{\omega}$ being the oscillation period. The third column depicts the mode structure at the same triangular cross-section ($\varphi = 36^{\circ}$) for 1/4th of the oscillation cycle. At $t = 0$ the mode structure corresponds to a 4/4 asymmetrically coupled DTM with weak 1/1 resistive kink part in the plasma centre. At $t = \frac{1}{4}T$, however, the mode structure is dominated by a 1/1 double tearing mode. The oscillation between the n^*=4 and the n^*=1 mode structures is visualized in the third column. There, the mode structure changes step by step from an n^*=4 to an n^*=1 double tearing mode within 1/4th of the oscillation period.

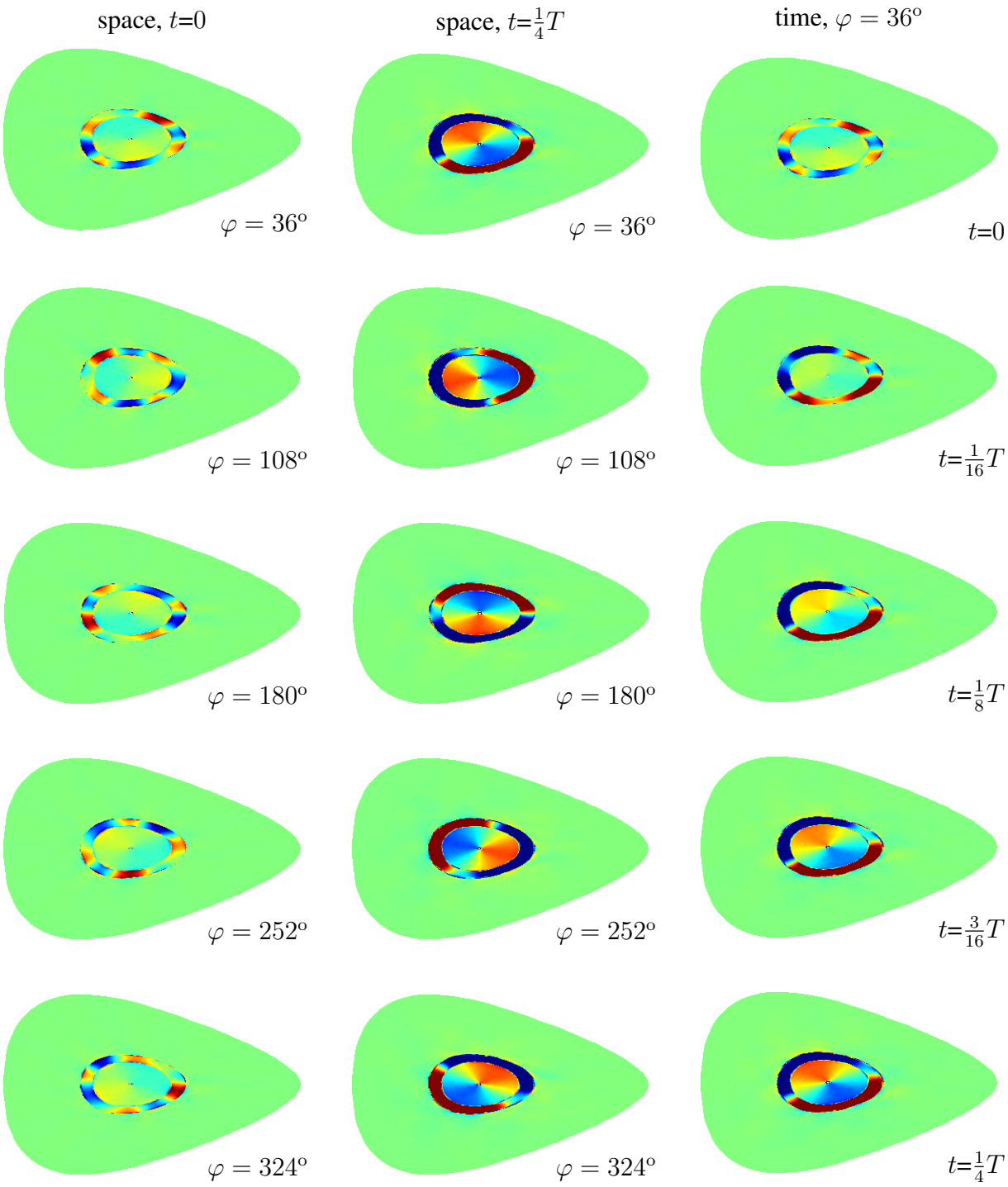

Figure 11: Oscillation between an n^*=4 and an n^*=1 double tearing mode structure. Growth rate and oscillation frequency amount to γ=4130 $\frac{1}{\mathrm{s}}$ and ω=207 $\frac{\mathrm{rad}}{\mathrm{s}}$ for η_a=$2 \cdot 10^{-8}$ Ωm, $\Delta s = 0.09$, and no viscosity.

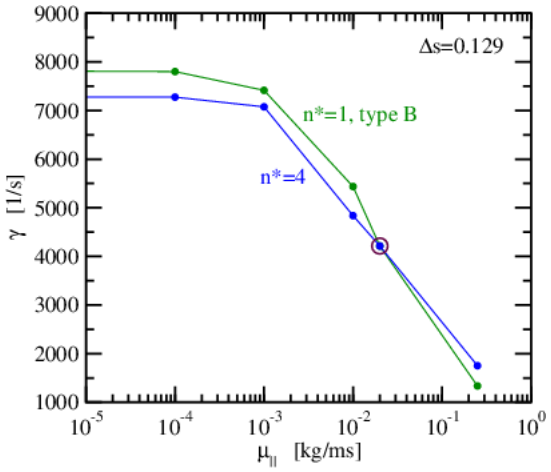

Figure 12: *Growth rates of the n^*=1 and the n^*=4 DTMs as functions of the parallel ion viscosity, $\mu_{||}$, for η_a=1 $\cdot$ 10^{-7} Ωm and Δs=0.129. The brown circle marks an overstable mode.*

Figure 12 shows the growth rates of the n^*=1 and the n^*=4 DTMs as functions of the parallel ion viscosity, $\mu_{||}$. The parallel viscosity has a negligible effect on both growth rates for $\mu_{||} \leq 1 \cdot 10^{-3}$ kg m^{-1}s^{-1}. For larger viscosity the growth rates quickly decrease. A very rough estimate of $\mu_{||} \approx \kappa_{||} v_i^{th} \rho_a / k_{||}$ yields a value of 0.24 kg m^{-1}s^{-1} for the considered low-β, collisionless equilibria. Here we used $\kappa_{||} = \sqrt{\pi}$, wave vector $k_{||} = 1/R_0$ (R_0=5.5 m being the major radius of W7-X), density $\rho_a = 8 \cdot 10^{-8}$ kg m^{-3}, and ion thermal velocity $v_i^{th} = 3.1 \cdot 10^5$ m s^{-1}. The latter corresponds to an ion temperature of $T_i = 1$ keV.

3.3 Mode family 2

In this section we study the stability properties of mode family 2. Figure 13 shows the growth rates of the n^*=2,3,7 and 8 DTMs as functions of the distance between the ι=1 flux surfaces. While the n^*=7 and n^*=8 modes are only unstable for small Δs, the growth rates of the n^*=2 and n^*=3 modes decrease for larger distances, but remain unstable. Again, overstable modes appear, when the growth rates of two n^*-types become equal. The frequencies of the n^*=2 $\leftrightarrow$ n^*=3 and the n^*=3 $\leftrightarrow$ n^*=8 oscillations are in the frequency range of 80-260 Hz.

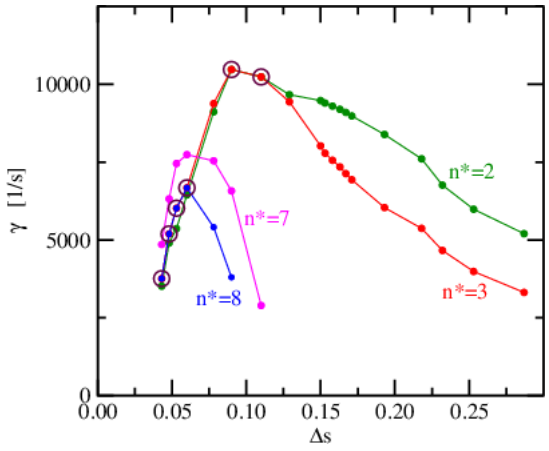

Figure 13: *Growth rates of the n^*=2,3,7 and 8 DTMs as functions of Δs, for $\eta_a = 1 \cdot 10^{-7}\,\Omega$m. The brown circles mark overstable modes.*

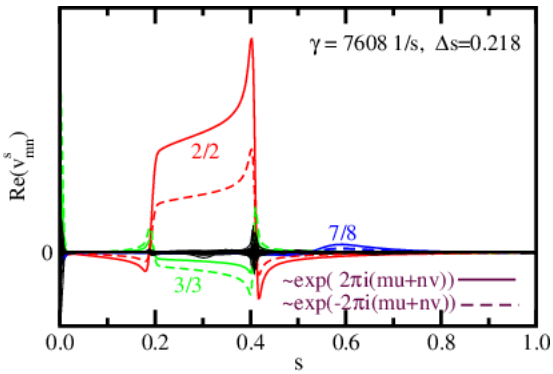

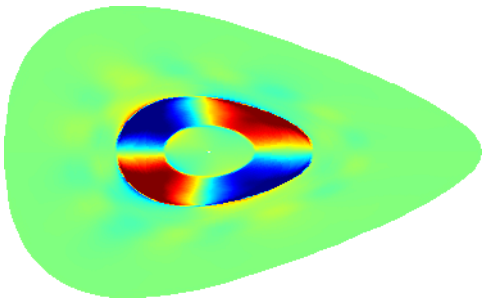

Figure 14: *Fourier harmonics and mode structure of the radial velocity perturbation of an n^*=2 DTM (Δs=0.218).*

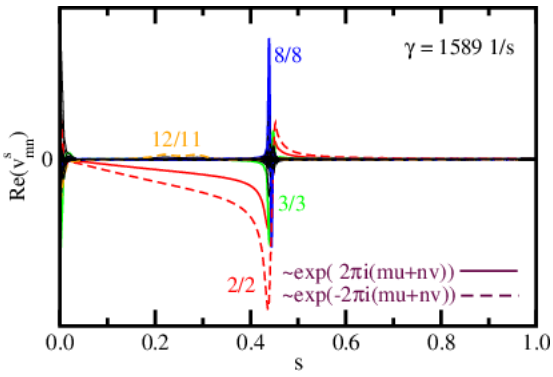

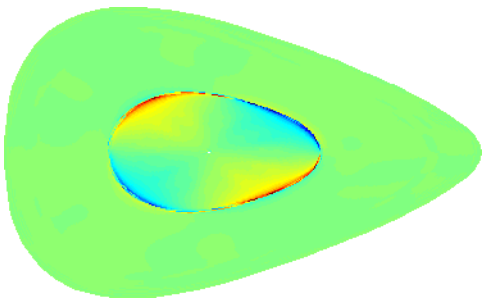

Figure 15: *Fourier harmonics and mode structure of the radial velocity perturbation of an n^*=2 single tearing mode (ι-profile 23, figure 3(b)).*

Fourier spectra and mode structures of the radial velocity perturbation of an n^*=2 double tearing (Δs=0.218) and a single tearing mode (ι-profile 23, figure 3(b)) are presented in figures 14 and 15, respectively. Particularly, n/m=2/2, 3/3 and 7/8 harmonics contribute to the n^*=2 DTM, while n/m=2/2, 3/3, 8/8, and 12/11 harmonics couple mainly to the n^*=2 single tearing mode.

Because of the very flat rotational transform profile, the radial perturbation of the single TM extends up to the plasma centre.

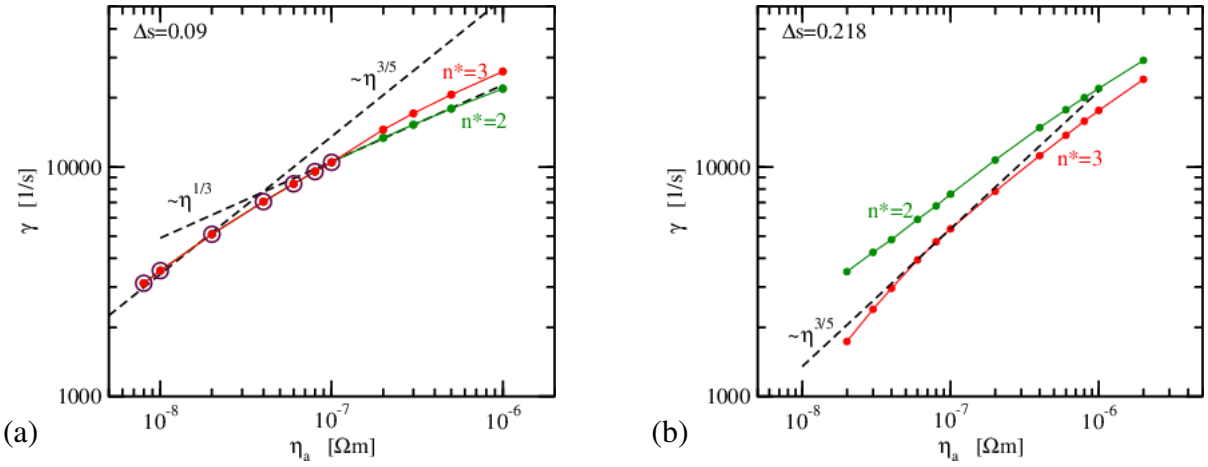

Figures 16: *Growth rates of the n^*=2 and 3 DTMs as functions of the plasma resistivity, η_a, for $\Delta s = 0.090$ (a), and $\Delta s = 0.218$ (b). The brown circles mark overstable modes, while the black dashed lines indicate the scalings $\gamma \propto \eta^{3/5}$, and $\gamma \propto \eta^{1/3}$.*

Figures 16(a)-(b) show the growth rates of the n^*=2 and 3 DTMs as functions of the plasma resistivity for Δs=0.09 (a), and Δs=0.218 (b). In case of the small Δs, the growth rates follow the $\gamma \propto \eta^{3/5}$ scaling for $\eta_a \lesssim 3 \cdot 10^{-8}$ Ωm, and the $\gamma \propto \eta^{1/3}$ scaling for $\eta_a \gtrsim 1 \cdot 10^{-7}$ Ωm. The modes become overstable for $\eta_a \leqslant 1 \cdot 10^{-7}$ Ωm. That is, these modes oscillate between the n^*=2 and n^*=3 mode structures in a frequency range of 85-150 Hz. In case of the large Δs only the $n^* = 3$ DTM follows the $\gamma \propto \eta^{3/5}$ scaling in a small resistivity range of $5 \cdot 10^{-8} \leqslant \eta_a \leqslant 5 \cdot 10^{-7}$ Ωm.

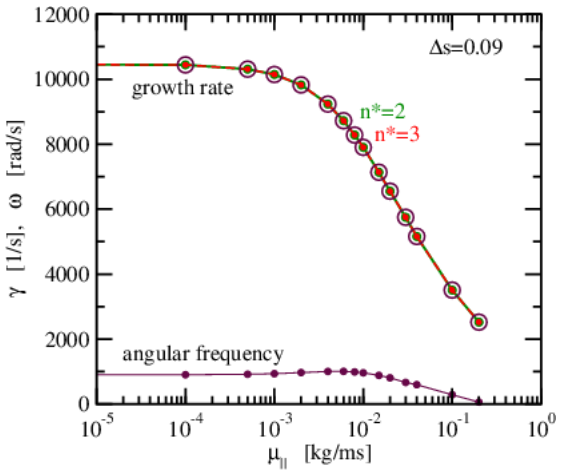

Figure 17: *Growth rate and angular frequency of an overstable DTM as function of $\mu_{||}$ for $\eta_a = 1 \cdot 10^{-7}$ Ωm, and Δs=0.09. The mode oscillates between the n^*=2 and n^*=3 mode structures in a frequency range of $10 \lesssim \nu \lesssim 160$ Hz.*

Figure 17 depicts growth rate and angular frequency of an n^*=2 $\leftrightarrow$ n^*=3 oscillating mode as function of the parallel viscosity, $\mu_{||}$. While the growth rate decreases quickly for $\mu_{||} > 1 \cdot 10^{-3}$ kg m^{-1}s^{-1}, the angular frequency is almost unchanged for $\mu_{||} \leqslant 1 \cdot 10^{-2}$ kg m^{-1}s^{-1}. For larger $\mu_{||}$, it also decreases.

4 Summary and conclusions

Comprehensive linear stability studies of resistive MHD modes were performed for W7-X-type equilibria with external current drive. For this purpose, sets of non-monotonic rotational transform profiles with one or two ι=1 flux surfaces were designed to simulate central co-ECCD. Stability studies were made for the corresponding equilibria using the 3D linear stability CASTOR3D code. The stability properties of all three mode families of these five-periodic equilibria were investigated in dependence of plasma resistivity, parallel ion viscosity, and distance between the ι=1 flux surfaces. Single and double tearing modes, resistive kink modes, and overstable DTMs, but no ideal kink modes could be found for these low-β equilibria. The overstable DTMs are exponentially growing modes with a mode structure oscillating between two n^*-types. Overstable modes occur for these 3D equilibria, when the growth rates of two different n^*-type modes of the same mode family are equal. The computed frequencies are in the range of ≈10-260 Hz. These frequencies are well below the experimentally observed precursor oscillations which have been observed before the thermal quench and which are in kHz range [27]. Scans of the growth rates with respect to viscosity showed a stabilizing effect of the parallel ion viscosity for $\mu_{||} \gtrsim 1 \cdot 10^{-3}$ kg m^{-1}s^{-1}. The growth rates of all investigated mode types rise with increasing resistivity. Depending on resistivity range, distance between the ι=1 flux surfaces, and n^*-type, some of the DTMs show a $\gamma \propto \eta^{3/5}$ or $\gamma \propto \eta^{1/3}$ scaling. The dependence of the scaling behaviour taking viscosity into account was not investigated.

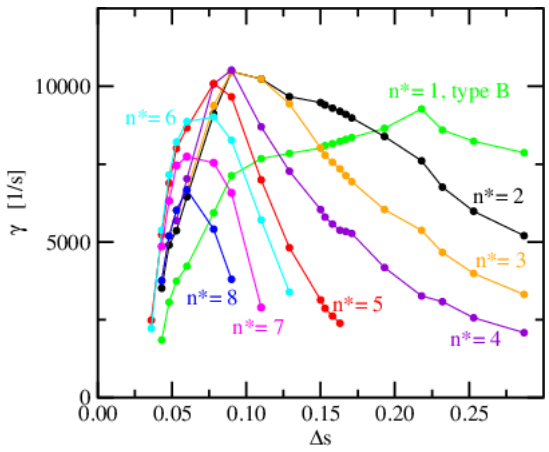

Figure 18: Growth rates of the n^*=1,2,...,8 DTMs as function of Δs for $\eta_a = 1 \cdot 10^{-7}$ Ωm taking no viscosity into account.

Figure 18 summarizes results obtained for the n^*=1,2,...,8 DTMs. The n^*-number of the most unstable resistive mode decreases with growing distance between the ι=1 flux surfaces. While the n^*=6 DTM is the most unstable mode for Δs=0.078, it is the n^*=1 mode for $\Delta s \geqslant 0.17$. The latter is also the most unstable mode for equilibria with only one ι=1 flux surface. With increasing Δs the character of the n^*=1 mode changes gradually from a DTM to a single TM or resistive kink mode, as shown in figure 9.

Sawtooth-like oscillations followed by a rapid decrease of the electron temperature were observed in W7-X discharges with ECCD [4]. The temporal evolution of the current density during co-ECCD led to an increase of the distance between the ι=1 flux surfaces and, finally, to ι-profiles with only one ι=1 flux surface [2]. The CASTOR3D code is a linear code and, therefore, it can not describe sawtooth oscillations. However, it describes the 3D geometry of Wendelstein 7-X correctly, and it shows that the n^*=1 resistive kink mode is the most unstable mode for either a large distance between the ι=1 flux surfaces, or a single ι=1 surface. Furthermore, non-linear resistive stability studies performed with the two-fluid TM1 code yielded two types of temperature crashes [28]. Assuming large aspect ratio (the Wendelstein 7-X aspect ratio is large enough) and circular cross-sections, but the same iota-profiles as the here considered Wendelstein 7-X type equilibria, partial and full temperature crashes were obtained depending on the distance between the ι=1 surfaces and the maximum ι-value. Last but not least, there is experimental evidence [27] that n=1 perturbations are involved in the observed sawtooth-like oscillations followed by a thermal quench in W7-X. In fact, 3D non-linear stability studies are required for a self-consistent description of sawtooth events in stellarators. However, the combination of the numerical results of 3D linear stability studies, and two-fluid, resistive, non-linear computations performed for simplified geometry supports together with experimental observations the picture of low-n resistive modes causing sawtooth oscillations followed by a thermal crash.

In a tokamak device a thermal quench is the first step of a disruption [20]. It causes an increase of the plasma resistivity followed by the ohmic dissipation of the plasma current. The fast decay of the huge plasma current of a tokamak releases a large amount of magnetic energy and leads to a complete breakdown of the magnetic confinement. In almost current-free stellarators, such as W7-X, confining nested flux surfaces are almost completely generated by currents in external coils. There, a thermal quench does not cause a loss of huge amount of magnetic energy, a breakdown of the confining magnetic field, or a severe damage of the device. That is, a discruption does not occur. One should also keep in mind that such thermal quenches are not typical for the stellarator Wendelstein 7-X, they are a consequence of the specific modifications of the ι-profile by external current drive.

Acknowlegements

The authors would like to thank Karl Lackner and Qingquan Yu for useful discussions.

This work has been carried out within the framework of the EUROfusion Consortium and has received funding from the Euratom research and training program 2014-2018 and 2019-2020 under grant agreement No 633053. The views and opinions expressed herein do not necessarily reflect those of the European Commission.

Appendix: Numerical details

(a) *Rotational transform profiles*

Adding to the monotonic rotational transform profile of the current-free equilibrium, $\iota_0(S)$, an analytical function

$$\iota(S) = \iota_0(S) + a_0 \exp\left(-\left(\frac{S-a_1}{a_2}\right)^2\right), \tag{2}$$

two sets of ι-profiles are created by varying the parameters a_0, a_1 and a_2. Here, equation (2) is formulated as function of the normalized toroidal flux, S, because the VMEC equilibrium code [19] uses S as radial coordinate. Varying the parameters a_0 and a_2 within the ranges $0.139 \leq a_0 \leq 0.23$ and $0.06 \leq a_2 \leq 0.09$ while keeping $a_1 = 0.10$ fixed, the first set of profiles (1-18) is obtained. In case of the second set (19-23) the parameter $a_0 = 0.23$ is kept fixed, while the parameters a_1 and a_2 are varied in the ranges $0.09 \leq a_1 \leq 0.06$, and $0.090 \leq a_2 \leq 0.180$.

(b) *Radial grid*

The eigenfunctions used in the CASTOR3D code are represented by Fourier series in poloidal and toroidal direction, and finite elements in radial direction [23]. Figure 19(a) shows the growth rates of n^*=1,4 and 6 double tearing modes as functions of Δs for $\eta_a = 1 \cdot 10^{-7}$ Ωm. The computations have been performed for an equidistant (100 grid points), and a non-equidistant radial grid (105 grid points). In case of the non-equidistant grid, the grid points are accumulated around the ι=1 flux surfaces. The minimum grid size amounts to 0.0005, and it increases up to 0.0133 with growing distance from these surfaces as illustrated in figures 19(b)-(d). There, the Fourier spectra of the real part of the radial velocity perturbation are shown for the n^*=4 mode with the red full circles indicating the locations of the radial grid points.

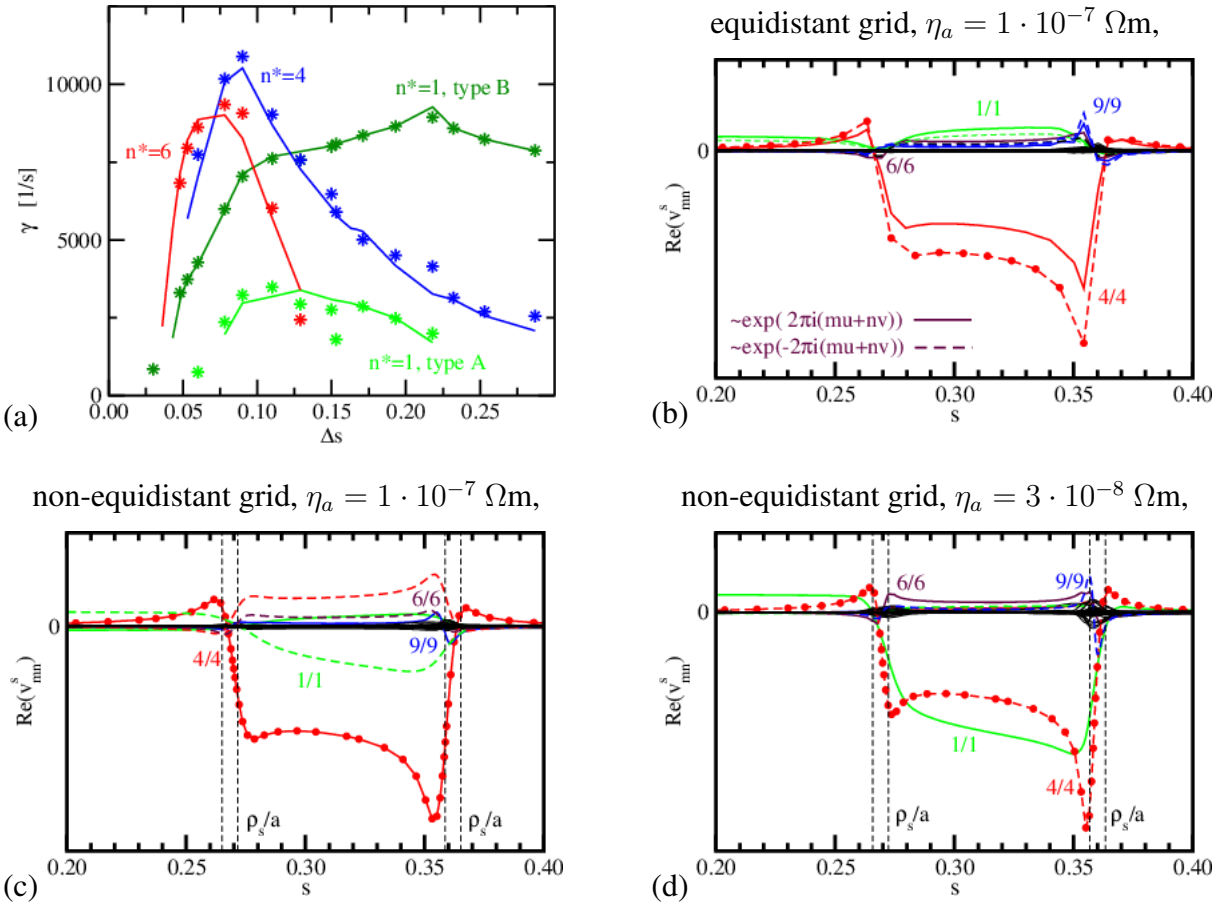

Figure 19: *(a) Growth rates of the n^*=1,4, and 6 resistive modes as functions of Δs for $\eta_a = 1 \cdot 10^{-7}$ Ωm and no viscosity. Computations performed with the equidistant radial grid are marked by stars, while the solid lines denote the results obtained with the non-equidistant grid. (b)-(d) Fourier spectra of the real part of the radial velocity perturbation of the n^*=4 mode for $\Delta s = 0.09$. The red full circles represent the locations of the radial grid points. The pairs of vertical dashed lines illustrate the width of the normalized ion sound Larmor radius, ρ_s/a.*

While in case of the non-equidistant grid the growth rates as function of Δs form smooth curves (solid lines in figure 19(a)), the values scatter around these curves for the equidistant grid (stars in figure 19(a)). This indicates that the grid points of the equidistant grid are not sufficient to describe the eigenfunctions accurately around the $\iota = 1$ flux surfaces, because the distance between the grid points is already comparable to the resistive layer width of the mode. The non-equidistant grid, however, works well even for smaller resistivities as shown in figures 19(c) and (d).

As already discussed in section 3, two-fluid effects become important if the ion sound Larmour radius, ρ_s, becomes comparable or larger than the resistive layer width. Assuming an electron

temperature of T_e=3 keV, the normalized radius amounts to $\rho_s/a \approx 0.007$ for Deuteron ions and $a = 0.5$ being the minor radius of W7-X. As indicated by the pairs of vertical dashed lines in figures 19(b) and (c), ρ_s becomes comparable to the resistive layer width for $\eta_a \lesssim 3 \cdot 10^{-8}\Omega$m in case of the considered n^*=4-type DTM. This is of course a rough estimate only.

(c) *Fourier spectra of the perturbations*

The Fourier spectra of the perturbations used for the linear stability studies are listed in table 1(a)-(c). Summarizing all harmonics of a mode family, in total 91, 92 and 90 Fourier harmonics are used for the mode families 0,1 and 2. The number of m's has been increased with growing n, because the higher the n, the more rational values of this kind are included in the ι-profiles. These harmonics are sufficient to obtain well converged results for the considered low-n^* modes.

Table 1a: mode family 0

n	m-interval
0	$0 \leq m \leq 10$
5	$-1 \leq m \leq 11$
10	$3 \leq m \leq 17$
15	$8 \leq m \leq 22$
20	$10 \leq m \leq 28$
25	$16 \leq m \leq 34$

Table 1b: mode family 1

n	m-interval
1	$-4 \leq m \leq 6$
4	$-2 \leq m \leq 10$
6	$-1 \leq m \leq 13$
9	$1 \leq m \leq 17$
11	$3 \leq m \leq 19$
14	$5 \leq m \leq 23$

Table 1c: mode family 2

n	m-interval
2	$-3 \leq m \leq 7$
3	$-3 \leq m \leq 9$
7	$0 \leq m \leq 14$
8	$1 \leq m \leq 15$
12	$4 \leq m \leq 20$
13	$4 \leq m \leq 22$

References

[1] KLINGER, T., ALONSO, A., BOZHENKOV, S., et al., Plasma Physics and Controlled Fusion **59** (2017) 014018.

[2] WOLF, R. C., ALI, A., ALONSO, A., et al., Nucl. Fusion **57** (2017) 102020.

[3] ERCKMANN, V., BRAND, P., BRAUNE, H., et al., Fusion Science and Technology **52** (2007) 291.

[4] WOLF, R. C., ALONSO, A., AKASLOMPOLO, S., et al., Phys. Plasmas **26** (2019) 082504.

[5] GRIEGER, G., LOTZ, W., MERKEL, P., et al., Phys. Fluids B **4** (1992) 2081.

[6] CHU, M. S., GREENE, J. M., JENSEN, T. H., MILLER, R. L., and BONDESON, A., Phys. Plasmas **2** (1995) 2236.

[7] VILLONE, F., LUI, Y., RUBINACCI, G., and VENTRE, S., Nuclear Fusion **50** (2010) 125011.

[8] CHAPMAN, I. T., SHARAPOV, S. E., HUYSMANS, G. T. A., and MIKHAILOVSKII, A. B., Phys. Plasmas **13** (2006) 062511.

[9] HUYSMANS, G. T. and CZARNY, O., Nuclear Fusion **47** (2007) 659.

[10] JARDIN, S. E. A., J. Comp. Phys. **200** (2004) 133.

[11] LÜTJENS, H. E. A., J. Comp. Phys. **227** (2008) 6944.

[12] NÜHRENBERG, C., Phys. Plasmas **3** (1996) 2401.

[13] ANDERSON, D. V., COOPER, W. A., GRUBER, R., MERAZZI, S., and SCHWENN, U., Int. J. Supercomput. Appl. **4** (1990) 34.

[14] NÜHRENBERG, C., Nuclear Fusion **56** (2016) 076010.

[15] NÜHRENBERG, C., private communication .

[16] MANICKAM, J., Nuclear Fusion **27** (1987) 1461.

[17] ZOCCO, A., MISHCHENKO, A., and KÖNIES, A., J. Plasma Phys. **85** (2019) 905850607.

[18] STRUMBERGER, E. and GÜNTER, S., Nuclear Fusion **59** (2019) 106008.

[19] HIRSHMAN, S. P. and WHITSON, J. C., Phys. Fluids **26** (1983) 3553.

[20] KIKUCHI, M., LACKNER, K., and TRAN, M. Q., *Fusion physics*, International Atomic Energy Agency, Vienna, 2012.

[21] DRAKE, J. F. and LEE, Y. C., Phys. Fluids **20** (1977) 1341.

[22] GÜNTER, S., SCHADE, S., MARASCHEK, M., et al., Nuclear Fusion **40** (2000) 1541.

[23] STRUMBERGER, E. and GÜNTER, S., Nuclear Fusion **57** (2017) 016032.

[24] HUYSMANS, G. T. A., GOEDBLOED, J. P., and KERNER, W., Phys. Fluids B **5** (1993) 1545.

[25] KERNER, W., GOEDBLOED, J. P., HUYSMANS, G. T. A., POEDTS, S., and SCHWARZ, E., J. Comput. Phys. **142** (1998) 271.

[26] GOEDBLOED, H. and POEDTS, S., *Principles of Magnetohydrodynamics*, Cambridge University Press, Cambridge, 2004.

[27] ZANINI, M., LAQUA, H. P., THOMSEN, H., et al., Nuclear Fusion, accepted for publication (2020).

[28] YU, Q., STRUMBERGER, E., IGOCHINE, V., et al., Nuclear Fusion **60** (2020) 076024.